

Electronic Structure and Resonant Circular Dichroism of $\text{La}_{0.7}\text{Sr}_{0.3}\text{MnO}_3$ from Soft X-ray Angle-Resolved Photoemission

Øyvind Finnseth,¹ Damian Brzozowski,¹ Anders Christian Mathisen,² Stefanie Suzanne Brinkman,² Xin Liang Tan,² Fabian Göhler,² Benjamin A. D. Williamson,¹ Kristoffer Eggestad,¹ Meng-Jie Huang,³ Jens Buck,^{4,3} Moritz Hoesch,⁵ Kai Rossnagel,^{6,3} Sverre M. Selbach,¹ Hendrik Bentmann,² and Ingrid Hallsteinsen¹

¹*Department of Materials Science and Engineering,
Norwegian University of Science and Technology, 7491 Trondheim, Norway*

²*Center for Quantum Spintronics, Department of Physics,
Norwegian University of Science and Technology, 7491 Trondheim, Norway*

³*Ruprecht Haensel Laboratory, DESY, 22607 Hamburg, Germany*

⁴*Institut für Experimentelle und Angewandte Physik,*

Christian-Albrechts-Universität zu Kiel, 24098 Kiel, Germany

⁵*Deutsches Elektronen-Synchrotron DESY, Notkestraße 85, 22607 Hamburg, Germany*

⁶*Institute of Experimental and Applied Physics, Kiel University, 24098 Kiel, Germany*

Coupling between spin, orbital, charge, and lattice degrees of freedom in transition-metal oxides produces a variety of electronic and magnetic phenomena of importance for future technologies. Here, we explore the electronic band structure of a (111)-oriented $\text{La}_{0.7}\text{Sr}_{0.3}\text{MnO}_3$ thin film through soft X-ray angle-resolved photoemission spectroscopy (ARPES). The measurements agree with the electronic band structure calculated with density functional theory using Hubbard U correction. Furthermore, we probe the circular dichroism in ARPES, and observe a pronounced momentum-resolved magnetic circular dichroism in resonant photoemission from the Mn L -edge. The approach combines the momentum- and spin-selectivity of ARPES and X-ray magnetic circular dichroism, respectively, which could provide a useful approach for the study of unconventional magnetism.

The coupling between charge, spin, orbital, and lattice degrees of freedom in transition-metal oxides (TMO) [1–3] gives rise to physical properties of scientific and technological interest, such as colossal magnetoresistance [4] and multiferroicity [5]. Through these degrees of freedom, tunable functionality may be achieved. Prominent examples include improving the transport properties of TMO-based transistors by interfacing with diamond [6], or amplifying magnetic frustration in La_2NiO_4 compressively strained by the substrate [7]. Specifically, recent work has focused on perovskite thin films grown in unconventional lattice orientations, exhibiting a wide range of properties not present in their bulk counterparts. These include enhanced interfacial conductivity [8], orbital patterning [9], and emergent magnetism [10].

In this context a well-studied TMO is $\text{La}_{0.7}\text{Sr}_{0.3}\text{MnO}_3$ (LSMO) with its room-temperature ferromagnetism, half-metallicity [11], and colossal magnetoresistivity [12], which have been studied for a variety of applications, such as magnetic tunnel junctions [13, 14], freestanding films [15, 16], and magnetoelectric memory [17]. In the case of LSMO thin films, the majority of the work has been focused on films in the pseudocubic (001) orientation, see, for example Refs. [18, 19]. However, films in the (111) orientation exhibit physical properties that are distinct from those in the (001) orientation. For instance, the magnetic anisotropy of (111)-oriented films is sixfold in-plane locally, with a prevailing isotropic macroscopic response [20], as compared to the biaxial in-plane magnetization of the (001)-oriented films [21]. Additionally, the magnetic domain sizes in (111)-oriented films is sig-

nificantly larger than those found in the (001) orientation [20]. Furthermore, interfacing LSMO with LaFeO_3 has been shown to induce ferromagnetic behavior in LaFeO_3 , with the induced magnetic moment an order of magnitude larger in the (111) orientation than in the (001) orientation [22, 23]. Finally, the insulating and magnetically inactive layer known to form at interfaces or surfaces in films of LSMO, often called the “dead layer”, is absent in (111)-oriented superlattices of LSMO and SrTiO_3 [24]. Despite this importance, experimental investigations of the electronic structure of (111)-oriented LSMO are lacking, with previous work only considering the (001) orientation [25–28].

In this work, we report soft X-ray angle-resolved photoemission (ARPES) measurements of (111)-oriented LSMO thin films, exploiting the increased bulk sensitivity at soft X-ray energies to probe the three-dimensional bulk electronic structure of LSMO. We support the interpretation of our experimental results by first-principles DFT+ U calculations. Furthermore, we study circular dichroism in ARPES for resonant excitation at the Mn L -edge and for non-resonant excitation. A pronounced magnetic CD (MCD) is observed in resonance, reflecting the ferromagnetic order of LSMO. At off-resonant energies, the MCD is found to be negligible.

EXPERIMENTAL DETAILS

A thin film of 6.2 nm of $\text{La}_{0.7}\text{Sr}_{0.3}\text{MnO}_3$ was grown epitaxially on a (111)-oriented SrTiO_3 substrate by pulsed

laser deposition. Samples were transferred under atmospheric conditions from the growth setup to the ultra-high vacuum photoemission setup. In order to obtain a chemically clean and ordered surface prior to the photoemission experiment, the sample was annealed at a temperature of ~ 640 K in O_2 gas with a partial pressure of 1×10^{-5} mbar, following previous work on the surface preparation of LSMO [29]. Successful surface preparation was confirmed by X-ray photoelectron spectroscopy and low-energy electron diffraction, indicating a clean, well-ordered surface after the preparation procedure. For details on sample growth and surface preparation, see Supplemental Material [30].

Soft X-ray ARPES measurements were conducted using the ASPHERE III end station at the variable polarization XUV beamline P04 of the PETRA III storage ring at DESY (Hamburg, Germany) [31]. ARPES data were collected at sample temperatures of approximately 30 K and pressures below 5×10^{-10} mbar. The energy resolution of the ARPES measurements was set to 75 meV. We used the angular deflection mode of the SCIENTA DA30-L analyzer, allowing for acquisition of angular distributions in a fixed sample geometry. Light incidence was within the analyzer slit plane at an angle of 20° to the sample surface [see Fig. 4(a)]. For all measurements, both left and right circularly polarized light was used. Unless otherwise stated, the results presented are obtained by taking the sum of the two different polarizations such that $I = I_L + I_R$. To mitigate effects of beam-induced damage to the thin film, the sample was moved so that a new spot was illuminated at 5 minute intervals.

COMPUTATIONAL DETAILS

Density functional theory (DFT) calculations were performed using VASP [32–34] to obtain the electronic band structure of LSMO. The effect of mixed occupancy of La and Sr was accounted for with supercells generated using the special quasirandom structure (SQS) method [35] as implemented in the `icet` Python package [36]. As a starting point for the supercell generation, a cubic $LaMnO_3$ primitive unit cell was expanded into a $4 \times 2 \times 2$ supercell with 80 atoms, out of which 11 La and 5 Sr, giving a stoichiometry of $La_{0.69}Sr_{0.31}MnO_3$.

The supercell geometry, including shape and volume, was optimized using a plane wave cutoff energy of 750 eV and a Γ -centered k -point grid of $2 \times 4 \times 4$ such that the forces acting on the ions were below 0.01 eV \AA^{-1} . The PBEsol functional [37] was used along with Dudarev’s [38] implementation of Hubbard U correction with $U = 3$ eV on Mn 3d [39, 40]. PBEsol+ U has been shown to yield good agreement with the structural properties of $LaMnO_3$ [41–43] and $SrMnO_3$ [44–46]. The $La(5s^25p^65d^16s^2)$, $Sr(4s^24p^65s^2)$, $Mn(3s^23p^63d^64s^1)$ and

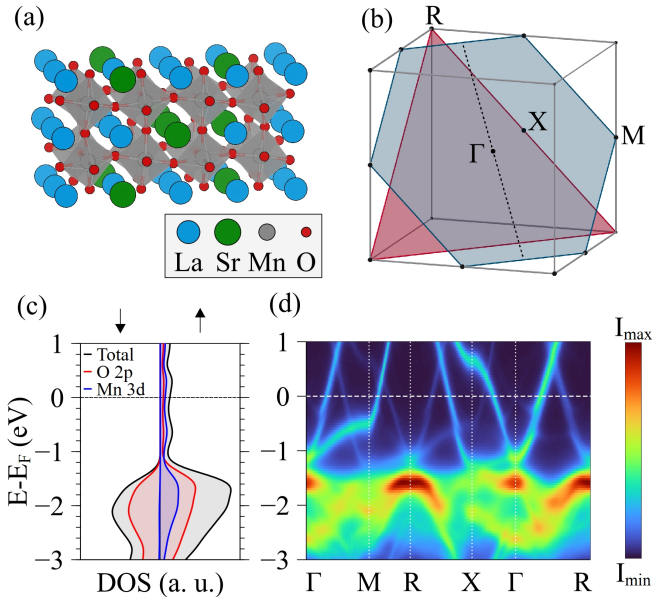


FIG. 1. (a) Supercell used in the DFT+ U calculations. (b) Diagram of the cubic Brillouin zone with high symmetry points indicated. (c) Density of states calculation for spin-up (left) and spin-down (right) electrons. All contributions besides O 2p and Mn 3d are negligible in the plotted range. (d) Unfolded spin-up band structure diagram calculated by DFT+ U .

$O(2s^22p^4)$ states were treated as valence electrons, while the interaction with the core states was accounted for using the projector-augmented wave method (PAW) [47].

To address band folding induced by supercell calculations, the `easyunfold` Python package [48] was used to obtain the unfolded band structure. The bands were unfolded onto a cubic primitive cell, and are thus expressed in a simple cubic coordinate system. In addition to obtaining unfolded band structures, this approach yields results with proper spectral weight, facilitating more direct comparison to ARPES measurements [49], as previously shown in e.g. Refs. [50, 51].

Fermi surfaces were obtained by calculating band structures using k -point grids with a spacing of approximately 0.02\AA^{-1} in the reciprocal planes of interest. The resulting band structures were unfolded onto the primitive cubic cell, and subsequently interpolated to construct continuous surface representations. The Fermi level in the DFT calculations was shifted to match the experimental results.

RESULTS AND DISCUSSION

Electronic structure of LSMO(111)

First we present the DFT results on the electronic structure of LSMO. The SQS-generated supercell is shown in Fig. 1(a). The calculated density of states (DOS) for this supercell, shown in Fig. 1(c), exhibits full spin polarization at the Fermi level, as expected for a half-metallic system. The unfolded spin-up electronic band structure is shown in Fig. 1(d) with high symmetry points as denoted in Fig. 1(b). Most prominent are the electron-like bands around the Γ point and the hole-like bands around the R point. There are, however, fainter hole-like states around the Γ point, and electron-like states around the R point as well. These are, in agreement with previous studies [25, 52], attributed to the tilting of the Mn octahedra causing a doubling of the unit cell along the [111] direction. This, in turn, causes backfolding between the R-X plane and the Γ -M plane [see Fig. 1(b)]. This interpretation is strengthened by the backfolded bands being absent for calculations conducted on the same supercell with the octahedral tilting removed (see Supplemental Material [30]).

Next we provide a comparison between the experimental and calculated electronic structure, focusing first on the dependence on out-of-plane momentum along the surface normal. In order to probe the out-of-plane momentum, a photon energy scan was conducted between energies of 300 eV and 530 eV. The orientation of the k_x -axis is denoted by the dashed line in Fig. 1(b), corresponding to the $[11\bar{2}]$ direction, while the out-of-plane direction k_z is along [111]. For conversion from photon energy to k_z , the free-electron final state approximation was used with an inner potential of $V_0 = 10$ eV [53]. With this inner potential, a Γ -point is located at $k_z = 11.2 \text{ \AA}^{-1}$.

The resulting cut through the Fermi surface, shown in Fig. 2(a), includes a larger hole-like pocket around the R point, and a smaller electron-like pocket around the Γ point, as expected from our band calculation in Fig. 1(d). The measured Fermi surface is in agreement with a calculation of the spin-up Fermi surface in the same cut through the Brillouin zone, shown in Fig. 2(b). As in Fig. 1(d), the unit cell doubling causes backfolding of bands between R and Γ . The backfolded bands are however not discernible in the experimental Fermi surface. Considering the low spectral weight the DFT calculations predict for these states, it is likely that they are too faint to resolve in the ARPES measurements. On the other hand it could indicate that the octahedral tilting in the LSMO thin film deviates from expected bulk pattern. This interpretation may be supported by reports of a region with varying A-cation distance persisting several nanometers from the interface in LSMO films grown on (111)-oriented SrTiO₃ [54], which could in turn influence

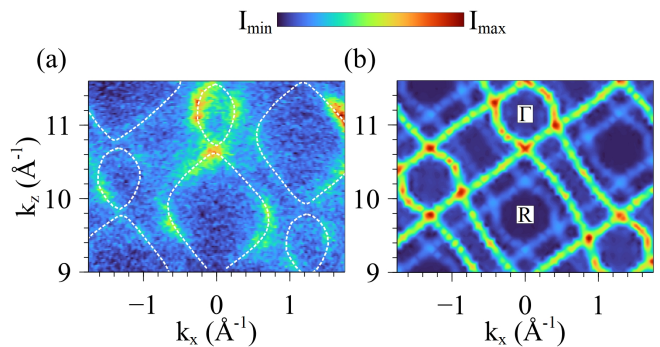


FIG. 2. (a) ARPES momentum map at the Fermi level along the [111] (out-of-plane) direction k_z and the in-plane direction k_x along $[11\bar{2}]$ as indicated in Fig. 1(b). The data was obtained by varying the photon energy from $h\nu = 300$ eV to 530 eV. Two main features are observed: a large pocket around the R point, and a smaller pocket around the Γ point. Traces of these features are added as guides to the eye. (b) DFT+ U calculated Fermi surface along the same cut through the Brillouin zone as in (a).

the tilting pattern. Precisely measuring the octahedral tilt in thin films is, in general, challenging, but has recently been demonstrated for (001)-oriented LSMO films on various substrates [55].

The DFT calculations of the spin-up Fermi surface in the R-X and Γ -M high symmetry cuts are shown in Figs. 3(a) and (b), respectively, corresponding to the red and blue planes in Fig. 1(b). For the R-X cut in Fig. 3(a), we identify two main features: a central pocket, denoted as feature 1, and a point-like feature in sixfold coordination, denoted as feature 2. Considering the Γ -M cut in Fig. 3(b), we denote feature 3 as the central electron-like pocket, and feature 4 as the surrounding triangular features. By comparing the Fermi surface cuts to the calculated band dispersion along the R-X and Γ -M direction in Figs. 3(c) and (d), features 1 and 3 are identified with the hole-like and electron-like states surrounding the R and Γ points, respectively. We furthermore observe that features 1 and 2 are replicated in the Γ -M cut, as well as features 3 and 4 in the R-X cut. This is attributed to the unit cell doubling along [111] mapping the Γ -M plane to the R-X plane, and vice versa. This mapping may also be seen in the fainter band dispersion in Figs. 3(c) and (d).

The DFT calculated band structure in Figs. 3(a)-(d) may be directly compared to the band structure obtained by ARPES, shown in Figs. 3(e)-(h). From the photon energy scan in Fig. 2 (a), $h\nu = 369$ eV and $h\nu = 475$ eV are identified as suitable photon energies to approximately probe the R-X and Γ -M planes, respectively. In Fig. 3(e) a Fermi surface cut through the R-X plane is shown. We identify the hole-like R-pocket (feature 1), the six-fold coordination of the R-points in the second Brillouin zone, and the point-like features (feature 2) as

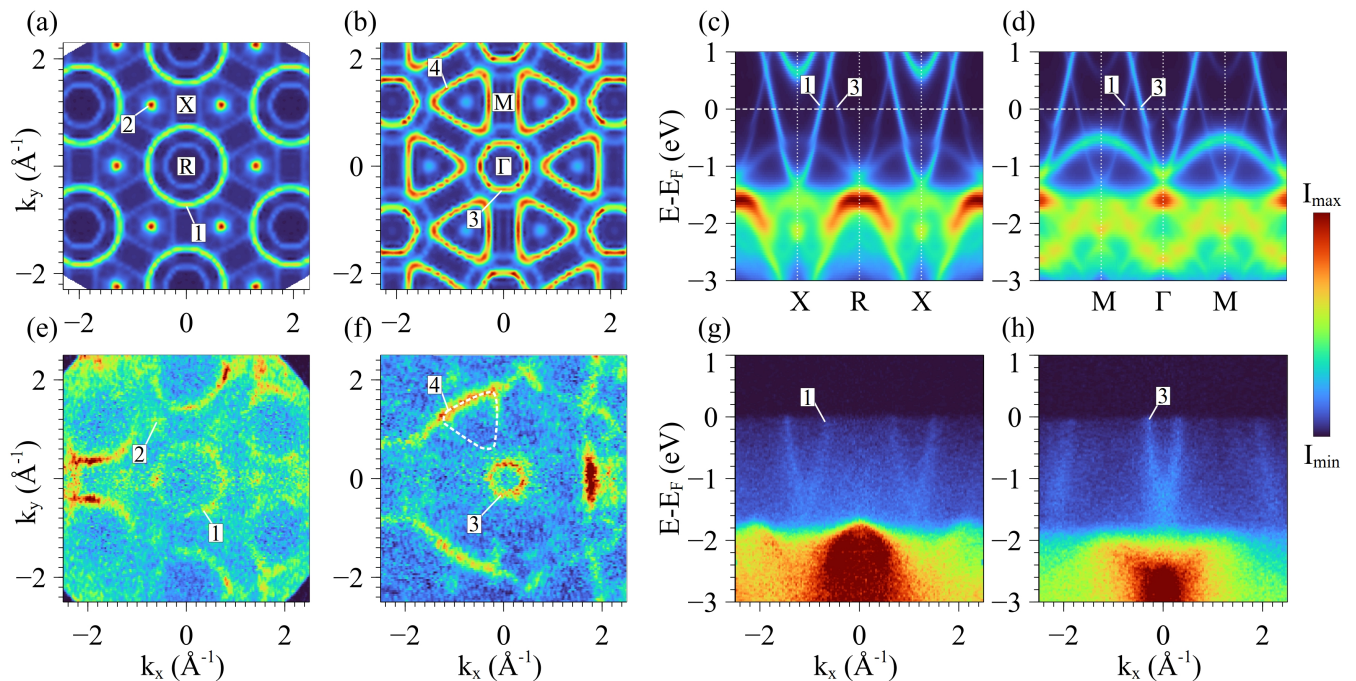


FIG. 3. Fermi surface cuts calculated by DFT+ U for the (a) R-X and (b) Γ -M high symmetry planes [cf. Fig. 1(b)]. The labels (1-4) denote the most prominent features in each of the Fermi surface cuts. Calculated valence band dispersions along the (c) R-X and (d) Γ -M directions. Bands crossing the Fermi level are marked according to the labels in (a) and (b). ARPES momentum maps at the Fermi level taken in the (e) R-X high symmetry plane, obtained with a photon energy of $h\nu = 369$ eV, and in the (f) Γ -M high symmetry plane, obtained with a photon energy of $h\nu = 475$ eV. Measured band dispersions along the R-X and Γ -M directions are shown in (g) and (h), respectively. The features identified in the DFT+ U calculations are indicated by the corresponding labels in (e)-(h). In (f), a trace of feature 4 from the DFT+ U calculation is overlaid as a guide to the eye.

predicted by DFT calculations in Fig. 3(a). For the Γ -M plane, depicted in Fig. 3(f), we similarly observe the central electron-like pocket (feature 3) and the edges of the surrounding feature 4. Beyond this, however, the Fermi surface cut as measured by ARPES shows a trifold modulation that is not present in the calculated Fermi surface. This is attributed to a modulation of the photoemission intensity due to the trifold symmetry along the [111] axis.

Figures 3(g) and (h) show the valence band dispersions along the R-X and Γ -M directions, respectively. As with the Fermi surface cuts in Figs. 3(e), (f), we observe features 1 and 3 in good agreement with the theoretical band dispersions. However, the dome-like band along the Γ -M direction predicted by DFT in Fig. 3(d) is not discernible in the ARPES measurement of Fig. 3(h). Furthermore, the backfolded bands due to unit cell doubling are not visible in neither the measured Fermi surface cuts nor the band dispersions. In sum, all features present in the experimental band structure measurements are accurately reproduced by the DFT+ U calculations, while some features predicted in the DFT+ U calculations, such as the backfolded bands, are not observed in the ARPES measurements.

Magnetic circular dichroism in resonant ARPES

We explored circular dichroism (CD) in resonant ARPES at the Mn L X-ray absorption edge as a momentum-resolved probe of spin polarization in the electronic band structure [56, 57]. Conceptually, the approach can be viewed from two sides: (i) as a regular CD-ARPES experiment but performed in resonance or (ii) as an X-ray magnetic circular dichroism (XMCD) experiment but with additional momentum resolution.

We start the discussion with a few general considerations. The CD-ARPES measurements were performed with the plane of light incidence (xz) aligned with a crystallographic mirror plane [112] along $k_y = 0$, as indicated in Fig. 4(a). The CD signal is obtained as the difference between photoemission intensities measured with left- and right circularly polarized photons, $I_{CD} = I_L - I_R$ [58]. In the absence of magnetic ordering, the crystallographic mirror plane imposes an antisymmetric CD angular distribution $I_{CD}(k_y) = -I_{CD}(-k_y)$ [59], resulting in a net zero angle-integrated CD signal. Note that the latter is also enforced by time-reversal symmetry even for incidence off the mirror plane. The symmetry-breaking by ferromagnetic order lifts these requirements, allowing

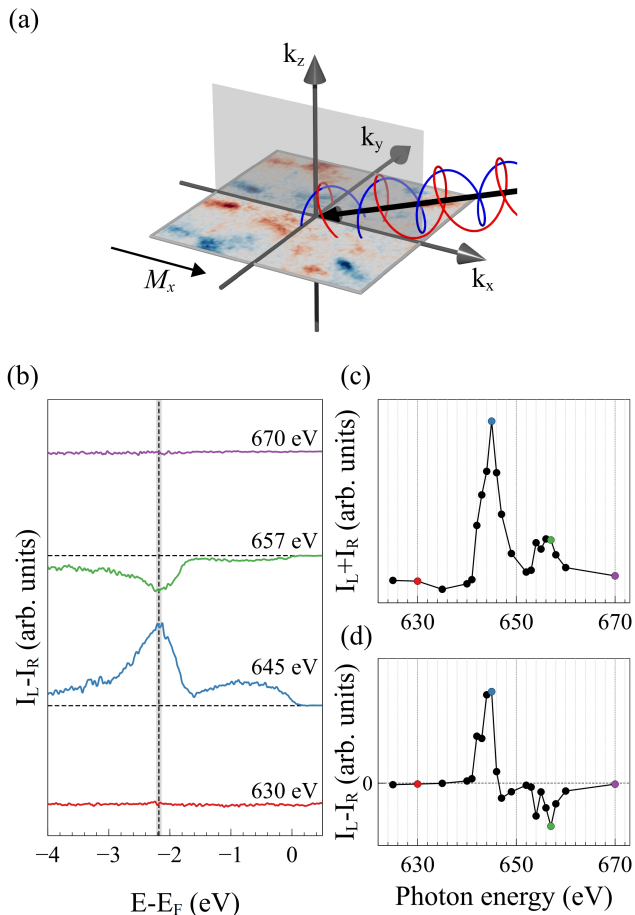


FIG. 4. (a) Experimental geometry of the measurements probing the circular dichroism in ARPES. The photons, either left or right circularly polarized, impinge on the sample along the black arrow at an incidence angle of 20° . The plane of light incidence is in the xz plane, shown in gray, which coincides with the mirror plane along the $[11\bar{2}]$ crystallographic axis. In this geometry, a magnetization M_x is expected to induce magnetic circular dichroism. (b) Angle-integrated CD ($I_{CD} = I_L - I_R$) in photoemission measured at photon energies before, on, and after the Mn L_3 and L_2 resonances. (c) Angle-integrated photoemission intensity ($I = I_L + I_R$) as a function of photon energy at $E - E_F = -2.18$ eV integrated over a range of 0.1 eV, as indicated by the vertical dashed line and shaded area in (b). (d) Angle-integrated CD as a function of photon energy at $E - E_F = -2.18$ eV integrated over a range of 0.1 eV. The photon energies depicted in (b) are highlighted by their respective colors in (c) and (d).

for non-zero net CD in photoemission, known as magnetic circular dichroism (MCD) in photoemission [60, 61]. The appearance of MCD, however, relies on spin-orbit interaction and usually is a small effect. Spin-orbit interaction in the photoexcitation process can be enhanced by tuning the photon energy to a resonant absorption edge, leading to pronounced MCD in angle-integrated resonant photoemission [62, 63]. This effect is closely related to the XMCD technique, the main difference being

that in XMCD, typically the full photoexcitation cross section is monitored (total electron yield). MCD and resonant photoemission may then be combined with angle-resolved photoelectron detection, yielding MCD in resonant ARPES, which naturally combines local magnetic and itinerant band-structure information [64] but to our knowledge has rarely been explored experimentally.

We first consider angle-integrated resonant photoemission experiments for LSMO(111). Figures 4(b)-(d) show the photoemission intensity within the plane of light incidence, integrated over an angular range of $\pm 15^\circ$ around normal emission. As the photon energy is tuned across the Mn $L_{3,2}$ absorption edge, the photoemission intensity is amplified by resonant enhancement [65], as seen in Fig. 4(c). On resonance, we observe a pronounced MCD that reverses sign between the L_3 and L_2 edges, while only a negligible MCD is found off resonance. The photon-energy dependence of the MCD signal in Fig. 4(d) resembles the Mn $L_{3,2}$ XMCD signal in LSMO(111) measured in total electron yield mode (see supplemental material [30] or Ref. [66]). These findings confirm that the observed MCD in resonant photoemission is dominated by the XMCD selection rules [67], in agreement with recent theory [56], and may be regarded as a partial electron yield XMCD signal. Therefore, given the grazing-incidence experimental geometry, see Fig. 4(a), the observed MCD can be attributed to a magnetization M_x along the $[11\bar{2}]$ axis. This remanent magnetization was established without applying an external magnetic field, and appeared to be uniform across the sample. The $[11\bar{2}]$ axis is parallel to the step-edges of the thin film. Such a preferential magnetization along the step-edges is consistent with previous reports for LSMO thin films in both the (001) and (111) orientations [20, 68]. The magnetic origin of the MCD was confirmed by magnetizing the sample along $\pm M_x$, which induced a sign reversal in the MCD signal (see Supplemental Material [30]). As seen in Fig. 4(b), significant MCD is observed across the entire valence band. Overall, the data in Fig. 4 confirm a ferromagnetic state with in-plane anisotropy in the LSMO(111) film.

Figure 5 presents measurements of the MCD in resonant ARPES. Notably, the momentum distribution of the resonant photoemission intensity in Fig. 5(a) shows well-defined, sharp features, in agreement with previous work [25]. This demonstrates that the core-level absorption and subsequent participator Auger decay, which dominate the resonant photoemission intensity, form a momentum-selective process that probes itinerant Bloch states. The magnetization M_x breaks the mirror symmetry of the experimental geometry, allowing for deviations from the relations $I(k_y) = I(-k_y)$ and $I_{CD}(k_y) = -I_{CD}(-k_y)$ that are enforced for the intensity $I = I_L + I_R$ and the circular dichroism $I_{CD} = I_L - I_R$ in a fully mirror symmetric situation [69]. Indeed, the experimental data for both I and I_{CD} in Figs. 5(a)-(b) show clear sig-

natures of broken mirror symmetry. The intensity distribution in Fig. 5(a) shows higher intensities at positive k_y for most features, especially those at larger k_y , with some exceptions, where the intensity is higher at negative k_y . See for instance the features indicated by the white arrows. The CD momentum distribution in Fig. 5(b) shows marked deviations from a perfect anti-symmetry, with positive/red contributions outweighing negative/blue contributions. We note that for excitation energies off resonance, we observed mirror-symmetry preserving momentum distributions for the intensity and the circular dichroism within experimental uncertainty (see Supplemental Material [30]), which indicates that the non-resonant MCD [60] is weak in LSMO, at least in the soft X-ray regime. This finding also helps to rule out potential misalignment in the experimental setup, further supporting the magnetic origin of the observed mirror-symmetry breaking.

The net MCD in the angle-integrated data in Fig. 4 manifests in the momentum-resolved resonant CD data in Fig. 5 as a contribution that is symmetric with respect to the crystallographic mirror xz plane. We extract the anti-symmetric and symmetric contributions to the total circular dichroism and plot them in Figs. 5(c) and (d), respectively. The symmetric contribution constitutes the momentum distribution of the resonant MCD. While there is some variation in the size of the MCD for different features in the Fermi surface cut, the MCD shows a momentum structure that is largely inherited from the intensity distribution in Fig. 5(a).

Our experiments for LSMO(111) establish a sizable momentum-dependent MCD in resonant ARPES at the Mn $L_{3,2}$ Mn absorption edge. The approach combines the spin sensitivity of XMCD with the momentum sensitivity of ARPES. Such spectroscopic information is otherwise accessible only through spin-resolved ARPES, a methodology that remains experimentally challenging, particularly for complex momentum distributions [70, 71]. Our results support recent theory [56], which proposes MCD in resonant ARPES as a probe of unconventional magnetic states with even- or odd-parity spin momentum textures, such as altermagnetism [72] or p-wave magnetism [73].

CONCLUSIONS

In conclusion, we have explored the electronic structure of a (111)-oriented LSMO thin film through soft X-ray angle-resolved photoemission spectroscopy. By exploiting the intrinsically sharp definition of the out-of-plane momentum in the soft X-ray photon-energy regime, we probe the three-dimensional bulk electronic structure of LSMO. The measured electronic structure is compared to the results of first-principles calculations performed on an LSMO supercell generated through the SQS method,

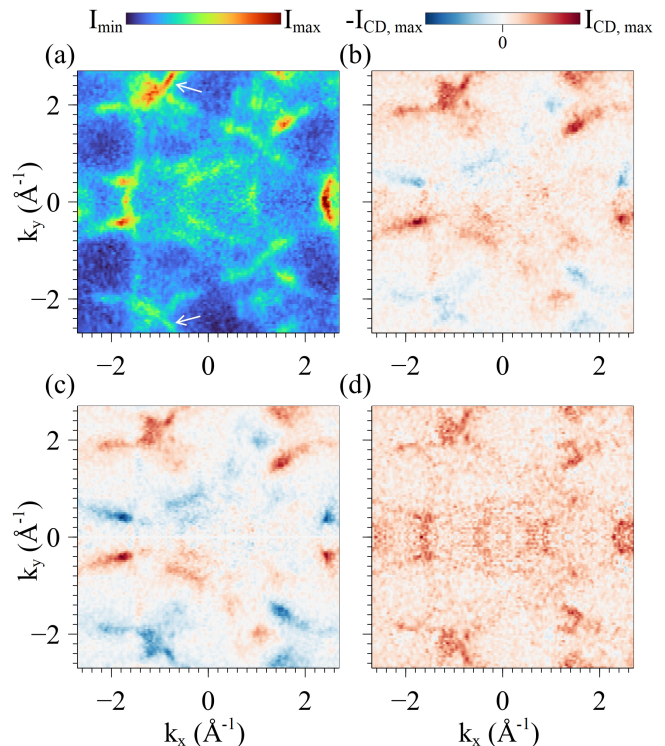


FIG. 5. ARPES data measured at the Fermi level ($E - E_F = 0$) with a photon energy $h\nu = 645$ eV tuned to the Mn L_3 resonance (cf. Fig. 4). (a) Total intensity obtained by taking the sum of left and right circularly polarized light, $I = I_L + I_R$. (b) Circular dichroism obtained by taking the difference between left and right circularly polarized light, $I_{CD} = I_L - I_R$. (c) Anti-symmetric contribution to I_{CD} extracted from (b), representing the geometrically induced circular dichroism. (d) Symmetric contribution to I_{CD} extracted from (b), representing the magnetically induced circular dichroism.

largely in agreement with the measured electronic structure.

Moreover, we have investigated the circular dichroism in on- and off-resonant ARPES, and find a significant, momentum-dependent MCD at the Mn $L_{3,2}$ resonance that is negligible at off-resonant energies. Combining spin- and momentum selectivity may enable new types of experiments probing unconventional magnetic materials [56].

ACKNOWLEDGMENTS

The authors acknowledge funding through the Research Council of Norway on the HONEYCOMB project (325063) and through the projects 323766, 302506, 354614, and 301954, and its Centres of Excellence funding scheme Grant No. 262633 “QuSpin.” F. G. was supported by the German Research Foundation (Deutsche Forschungsgemeinschaft, DFG) through Grant No. 556350547. Computational resources were provided

by Sigma2 under the project NN9264K. We acknowledge DESY (Hamburg, Germany), a member of the Helmholtz Association HGF, for the provision of experimental facilities. Parts of this research were carried out at PETRA III. Data were collected using the ASPHERE III instrument at beamline P04. Beamtime was allocated for proposal II-20230019. The ASPHERE III instrument is funded by the ErUM-Pro program (grant number 05K25FK4) of the German Federal Ministry of Research, Technology and Space (BMFTR). We would like to thank Frank Scholz and Jörn Seltmann for assistance in using beamline P04.

-
- [1] Y. Tokura and N. Nagaosa, Orbital physics in transition-metal oxides, *Science* **288**, 462 (2000).
- [2] H. Chen and D. Yi, Spin-charge conversion in transition metal oxides, *APL Materials* **9**, 60908 (2021).
- [3] T. Takayama, J. Chaloupka, A. Smerald, G. Khaliullin, and H. Takagi, Spin-Orbit-Entangled Electronic Phases in 4d and 5d Transition-Metal Compounds, *J. Phys. Soc. Jpn.* **90** (2021).
- [4] T. Kimura, Y. Tomioka, H. Kuwahara, A. Asamitsu, M. Tamura, and Y. Tokura, Interplane Tunneling Magnetoresistance in a Layered Manganite Crystal, *Science* **274**, 1698 (1996).
- [5] C. Ahn, A. Cavalleri, A. Georges, S. Ismail-Beigi, A. J. Millis, and J. M. Triscone, Designing and controlling the properties of transition metal oxide quantum materials, *Nat. Mater.* **20**, 1462 (2021).
- [6] Z. Yin, M. Tordjman, Y. Lee, A. Vardi, R. Kalish, and J. A. Del Alamo, Enhanced transport in transistor by tuning transition-metal oxide electronic states interfaced with diamond, *Sci. Adv.* **4** (2018).
- [7] I. Biało, L. Martinelli, G. De Luca, P. Worm, A. Drewnowski, S. Jöhr, J. Choi, M. Garcia-Fernandez, S. Agrestini, K. J. Zhou, K. Kummer, N. B. Brookes, L. Guo, A. Edgeton, C. B. Eom, J. M. Tomczak, K. Held, M. Gibert, Q. Wang, and J. Chang, Strain-tuned incompatible magnetic exchange-interaction in La_2NiO_4 , *Commun. Phys.* **7**, 230 (2024).
- [8] G. Herranz, F. Sánchez, N. Dix, M. Scigaj, and J. Fontcuberta, High mobility conduction at (110) and (111) $\text{LaAlO}_3/\text{SrTiO}_3$ interfaces, *Sci. Rep.* **2**, 758 (2012).
- [9] S. Middey, D. Meyers, D. Doennig, M. Kareev, X. Liu, Y. Cao, Z. Yang, J. Shi, L. Gu, P. J. Ryan, R. Pentcheva, J. W. Freeland, and J. Chakhalian, Mott Electrons in an Artificial Graphenelike Crystal of Rare-Earth Nickelate, *Phys. Rev. Lett.* **116**, 056801 (2016).
- [10] M. Gibert, P. Zubko, R. Scherwitzl, J. Íñiguez, and J. M. Triscone, Exchange bias in LaNiO_3 - LaMnO_3 superlattices, *Nat. Mater.* **11**, 195 (2012).
- [11] J. H. Park, E. Vescovo, H. J. Kim, C. Kwon, R. Ramesh, and T. Venkatesan, Direct evidence for a half-metallic ferromagnet, *Nature* 1998 392:6678 **392**, 794 (1998).
- [12] Z. Trajanovic, C. Kwon, M. C. Robson, K. C. Kim, M. Rajeswari, R. Ramesh, T. Venkatesan, S. E. Lofland, S. M. Bhagat, and D. Fork, Growth of colossal magnetoresistance thin films on silicon, *Appl. Phys. Lett.* **69**, 1005 (1996).
- [13] L. Samet, D. Imhoff, J. L. Maurice, J. P. Contour, A. Gloter, T. Manoubi, A. Fert, and C. Colliex, EELS study of interfaces in magnetoresistive LSMO/STO/LSMO tunnel junctions, *Eur. Phys. J. B* **34**, 179 (2003).
- [14] J. Pawlak, W. Skowroński, A. Żywczak, and M. Przybylski, Room-Temperature Multiferroicity and Magnetization Dynamics in Fe/BTO/LSMO Tunnel Junction, *Adv. Electron. Mater.* **8**, 2100574 (2022).
- [15] E. Brand, C. Hoegfeldt, A. Palliotto, I. V. Maznichenko, D. Rata, S. Ostanin, J. Chen, S. Lounis, K. Doerr, A. Ernst, S. Kadkhodazadeh, N. Pryds, and D.-S. Park, Epitaxial Strain Engineering of High-Quality Freestanding Single-Crystalline Complex Oxides, *ACS Nano* **19**, 41172 (2025).
- [16] Q. Du, W. Wang, X. Sun, J. Wu, Z. Hu, B. Tian, Q. Lv, Z. Wang, and M. Liu, Efficient electrical control of magnetization switching and ferromagnetic resonance in flexible $\text{La}_{0.7}\text{Sr}_{0.3}\text{MnO}_3$ films, *Nano Res.* **17**, 10017 (2024).
- [17] J. Li, L. Wu, M. Ma, R. Song, C. Dong, J. Wei, J. Li, X. Wang, and M. Li, Effect of annealing temperature on resistive switching behavior of $\text{Al}/\text{La}_{0.7}\text{Sr}_{0.3}\text{MnO}_3/\text{LaNiO}_3$ devices, *Curr. Appl. Phys.* **46**, 21 (2023).
- [18] H. Boschker, M. Huijben, A. Vailionis, J. Verbeeck, S. Van Aert, M. Luysberg, S. Bals, G. Van Tendeloo, E. P. Houwman, G. Koster, D. H. Blank, and G. Rijnders, Optimized fabrication of high-quality $\text{La}_{0.67}\text{Sr}_{0.33}\text{MnO}_3$ thin films considering all essential characteristics, *J. Phys. D* **44**, 205001 (2011).
- [19] M. Cesaria, A. P. Caricato, G. Maruccio, and M. Martino, LSMO – growing opportunities by PLD and applications in spintronics, *J. Phys.: Conf. Ser.* **292**, 012003 (2011).
- [20] I. Hallsteinsen, E. Folven, F. K. Olsen, R. V. Chopdekar, M. S. Rzchowski, C. B. Eom, J. K. Grepstad, and T. Tybell, Crystalline symmetry controlled magnetic switching in epitaxial (111) $\text{La}_{0.7}\text{Sr}_{0.3}\text{MnO}_3$ thin films, *APL Mater.* **3**, 62501 (2015).
- [21] L. M. Berndt, V. Balbarin, and Y. Suzuki, Magnetic anisotropy and strain states of (001) and (110) colossal magnetoresistance thin films, *Appl. Phys. Lett.* **77**, 2903 (2000).
- [22] I. Hallsteinsen, M. Moreau, A. Grutter, M. Nord, P. E. Vullum, D. A. Gilbert, T. Bolstad, J. K. Grepstad, R. Holmestad, S. M. Selbach, A. T. N'Diaye, B. J. Kirby, E. Arenholz, and T. Tybell, Concurrent magnetic and structural reconstructions at the interface of (111)-oriented $\text{La}_{0.7}\text{Sr}_{0.3}\text{MnO}_3/\text{LaFeO}_3$, *Phys. Rev. B* **94**, 201115 (2016).
- [23] F. Y. Bruno, M. N. Grisolia, C. Visani, S. Valencia, M. Varela, R. Abrudan, J. Tornos, A. Rivera-Calzada, A. A. Ünal, S. J. Pennycook, Z. Sefrioui, C. Leon, J. E. Villegas, J. Santamaria, A. Barthélémy, and M. Bibes, Insight into spin transport in oxide heterostructures from interface-resolved magnetic mapping, *Nat. Commun.* **6**, 6306 (2015).
- [24] E. J. Guo, M. A. Roldan, T. Charlton, Z. Liao, Q. Zheng, H. Ambaye, A. Herklotz, Z. Gai, T. Z. Ward, H. N. Lee, and M. R. Fitzsimmons, Removal of the Magnetic Dead Layer by Geometric Design, *Adv. Funct. Mater.* **28**, 1800922 (2018).
- [25] L. L. Lev, J. Krempaský, U. Staub, V. A. Rogalev, T. Schmitt, M. Shi, P. Blaha, A. S. Mishchenko, A. A.

- Veligzhanin, Y. V. Zubavichus, M. B. Tsetlin, H. Volfová, J. Braun, J. Minár, and V. N. Strocov, Fermi Surface of Three-Dimensional La_{1-x}Sr_xMnO₃ Explored by Soft-X-Ray ARPES: Rhombohedral Lattice Distortion and its Effect on Magnetoresistance, *Phys. Rev. Lett.* **114**, 237601 (2015).
- [26] K. Horiba, M. Kitamura, K. Yoshimatsu, M. Minohara, E. Sakai, M. Kobayashi, A. Fujimori, and H. Kumigashira, Isotropic Kink and Quasiparticle Excitations in the Three-Dimensional Perovskite Manganite La_{0.6}Sr_{0.4}MnO₃, *Phys. Rev. Lett.* **116**, 076401 (2016).
- [27] A. Chikamatsu, H. Wadati, H. Kumigashira, M. Oshima, A. Fujimori, N. Hamada, T. Ohnishi, M. Lippmaa, K. Ono, M. Kawasaki, and H. Koinuma, Band structure and Fermi surface of La_{0.6}Sr_{0.4}MnO₃ thin films studied by in situ angle-resolved photoemission spectroscopy, *Phys. Rev. B* **73**, 195105 (2006).
- [28] J. Krempaský, V. N. Strocov, L. Patthey, P. R. Willmott, R. Herger, M. Falub, P. Blaha, M. Hoesch, V. Petrov, M. C. Richter, O. Heckmann, and K. Hricovini, Effects of three-dimensional band structure in angle- and spin-resolved photoemission from half-metallic La_{2/3}Sr_{1/3}MnO₃, *Phys. Rev. B* **77**, 165120 (2008).
- [29] Å. F. Monsen, F. Song, Z. S. Li, J. E. Boschker, T. Tybell, E. Wahlström, and J. W. Wells, Surface stoichiometry of La_{0.7}Sr_{0.3}MnO₃ during in vacuo preparation; A synchrotron photoemission study, *Surf. Sci.* **606**, 1360 (2012).
- [30] See Supplemental Material at [URL to be inserted by publisher] for additional information on sample characterization, impact of octahedral tilt patterns, and circular dichroism.
- [31] J. Viehhaus, F. Scholz, S. Deinert, L. Glaser, M. Ilchen, J. Seltmann, P. Walter, and F. Siewert, The Variable Polarization XUV Beamline P04 at PETRA III: Optics, mechanics and their performance, *NIM A* **710**, 151 (2013).
- [32] G. Kresse and J. Hafner, Ab initio molecular dynamics for liquid metals, *Phys. Rev. B* **47** (1993).
- [33] G. Kresse and J. Furthmüller, Efficient iterative schemes for ab initio total-energy calculations using a plane-wave basis set, *Phys. Rev. B* **54** (1996).
- [34] G. Kresse and J. Furthmüller, Efficiency of ab-initio total energy calculations for metals and semiconductors using a plane-wave basis set, *Comput. Mater. Sci.* **6**, 15 (1996).
- [35] A. Zunger, S. H. Wei, L. G. Ferreira, and J. E. Bernard, Special quasirandom structures, *Phys. Rev. Lett.* **65**, 353 (1990).
- [36] M. Ångqvist, W. A. Muñoz, J. M. Rahm, E. Fransson, C. Durniak, P. Rozyczko, T. H. Rod, and P. Erhart, ICET – A Python Library for Constructing and Sampling Alloy Cluster Expansions, *Adv. Theory Simul.* **2**, 1900015 (2019).
- [37] J. P. Perdew, A. Ruzsinszky, G. I. Csonka, O. A. Vydrov, G. E. Scuseria, L. A. Constantin, X. Zhou, and K. Burke, Restoring the density-gradient expansion for exchange in solids and surfaces, *Phys. Rev. Lett.* **100**, 136406 (2008).
- [38] S. L. Dudarev, G. A. Botton, S. Y. Savrasov, C. J. Humphreys, and A. P. Sutton, Electron-energy-loss spectra and the structural stability of nickel oxide: An LSDA+U study, *Phys. Rev. B* **57**, 1505 (1998).
- [39] H. L. Hmok, E. Martínez-Aguilar, J. Ribas-Ariño, J. M. Siqueiros Beltrones, J. L. Sánchez Llamazares, and O. Raymond Herrera, Effect of La³⁺/Sr²⁺ ordering on the magnetic properties of La_{2/3}Sr_{1/3}MnO₃ by first principles calculations, *Comput. Mater. Sci.* **177**, 109575 (2020).
- [40] M. Moreau, S. M. Selbach, and T. Tybell, Octahedral coupling in (111)- and (001)-oriented La_{2/3}Sr_{1/3}MnO₃/SrTiO₃ heterostructures, *J. Appl. Phys.* **124**, 185301 (2018).
- [41] T. A. Mellan, F. Corà, R. Grau-Crespo, and S. Ismail-Beigi, Importance of anisotropic Coulomb interaction in LaMnO₃, *Phys. Rev. B* **92**, 085151 (2015).
- [42] J. H. Lee and B. Kim, Revisiting LaMnO₃: A density functional theory study, *Curr. Appl. Phys.* **78**, 7 (2025).
- [43] A. L. Gavin and G. W. Watson, Modelling the electronic structure of orthorhombic LaMnO₃, *Solid State Ionics* **299**, 13 (2017).
- [44] X. Zhu, A. Edström, and C. Ederer, Magnetic exchange interactions in SrMnO₃, *Phys. Rev. B* **101**, 064401 (2020).
- [45] A. Edström and C. Ederer, First-principles-based strain and temperature-dependent ferroic phase diagram of SrMnO₃, *Phys. Rev. Mater.* **2**, 104409 (2018).
- [46] A. Marthinsen, C. Faber, U. Aschauer, N. A. Spaldin, and S. M. Selbach, Coupling and competition between ferroelectricity, magnetism, strain, and oxygen vacancies in AMnO₃ perovskites, *MRS Commun.* **6**, 182 (2016).
- [47] G. Kresse and D. Joubert, From ultrasoft pseudopotentials to the projector augmented-wave method, *Phys. Rev. B* **59**, 1758 (1999).
- [48] B. Zhu, S. R. Kavanagh, and D. Scanlon, easyunfold: A Python package for unfolding electronic band structures, *J. Open Source* **9**, 5974 (2024).
- [49] W. Ku, T. Berlijn, and C. C. Lee, Unfolding First-Principles Band Structures, *Phys. Rev. Lett.* **104**, 216401 (2010).
- [50] O. Rubel, J. B. Moussy, P. Foulquier, and V. Brouet, Band unfolding with a general transformation matrix: From code implementation to interpretation of photoemission spectra, *Comp. Phys. Commun.* **291**, 108800 (2023).
- [51] J. I. Iwata, Y. I. Matsushita, H. Nishi, Z. X. Guo, and A. Oshiyama, Mining single-electron spectra of the interface states from a supercell band structure of silicene on an Ag(111) substrate with band-unfolding methodology, *Phys. Rev. B* **96**, 235442 (2017).
- [52] F. Y. Bruno, M. Gibert, and S. Mckeown Walker, Electronic structure of buried LaNiO₃ layers in (111)-oriented LaNiO₃/LaMnO₃ superlattices probed by soft x-ray ARPES, *APL Mater.* **5**, 16101 (2017).
- [53] A. Damascelli, Probing the electronic structure of complex systems by ARPES, *Phys. Scr.* **T109**, 61 (2004).
- [54] M. Nord, P. E. Vullum, I. MacLaren, T. Tybell, and R. Holmestad, Atomap: a new software tool for the automated analysis of atomic resolution images using two-dimensional Gaussian fitting, *Adv. Struct. Chem. Img.* **3**, 9 (2017).
- [55] J. K. Dey, K. Jagadish, A. Bandyopadhyay, S. Chowdhury, M. Hoesch, M. Valvidares, A. Ahlawat, F. Afaneh, A. Keshri, B. Roul, S. B. Krupanidhi, M. Gupta, R. J. Choudhary, T. Venkatesan, A. Narayan, N. Ravishankar, and S. Das, An unconventional pathway to correlate the octahedral tilt coupling and spin-orbit reconstruction at oxide interfaces, *Nat. Commun.* **17**, 332 (2025).
- [56] P. Krüger, Circular Dichroism in Resonant Photoelectron Diffraction as a Direct Probe of Sublattice Magnetization in Altermagnets, *Phys. Rev. Lett.* **135**, 196703 (2025).

- [57] R. Sagehashi, G. Park, and P. Krüger, Theory of circular dichroism in angle-resolved resonant photoemission from magnetic surfaces, *Phys. Rev. B* **107**, 075407 (2023).
- [58] D. Oh, H. Bentmann, and R. Comin, Interplay of orbital angular momentum and chirality, *Nature Physics* 2025, 1 (2025).
- [59] T. Figgemeier, M. Ünzelmann, P. Eck, J. Schusser, L. Crippa, J. N. Neu, B. Geldiyev, P. Kagerer, J. Buck, M. Kalläne, M. Hoesch, K. Rossnagel, T. Siegrist, L. K. Lim, R. Moessner, G. Sangiovanni, D. Di Sante, F. Reinert, and H. Bentmann, Imaging Orbital Vortex Lines in Three-Dimensional Momentum Space, *Phys. Rev. X* **15**, 011032 (2025).
- [60] W. Kuch and C. M. Schneider, Magnetic dichroism in valence band photoemission, *Rep. Prog. Phys.* **64**, 147 (2001).
- [61] P. Rosenberger, A. Darmawan, O. Fedchenko, O. Tkach, S. V. Chernov, D. Kutnyakhov, M. Hoesch, M. Scholz, K. Rossnagel, R. Pentcheva, G. Schönhense, H. J. Elmers, and M. Müller, Spin polarization of the two-dimensional electron gas at the EuO/SrTiO₃ (001) interface, *Phys. Rev. Mater.* **9**, 064401 (2025).
- [62] L. H. Tjeng, C. T. Chen, P. Rudolf, G. Meigs, G. Van Der Laan, and B. T. Thole, Magnetic circularly polarized 2p resonant photoemission of nickel, *Phys. Rev. B* **48**, 13378 (1993).
- [63] J. B. Goedkoop, N. B. Brookes, A. Bauer, E. Weschke, C. Schüssler-Langeheine, E. Navas, A. Mühlig, and G. Kaindl, Magnetic circular dichroism in Tb 3d 4f resonant photoemission, *Phys. Rev. B* **59**, 8835 (1999).
- [64] F. Da Pieve, Fingerprints of entangled spin and orbital physics in itinerant ferromagnets via angle-resolved resonant photoemission, *Phys. Rev. B* **93**, 035106 (2016).
- [65] M. Weinelt, A. Nilsson, M. Magnuson, T. Wiell, N. Wassdahl, O. Karis, A. Föhlisch, N. Mårtensson, J. Stöhr, and M. Samant, Resonant Photoemission at the 2pEdges of Ni: Resonant Raman and Interference Effects, *Phys. Rev. Lett.* **78**, 967 (1997).
- [66] A. Zakharova, M. Caputo, E. B. Guedes, M. Radovic, F. Nolting, and C. Piamonteze, Interplay between magnetism and interface-induced effects in ultrathin manganites, *Phys. Rev. Mater.* **5**, 124404 (2021).
- [67] Stöhr J, Exploring the microscopic origin of magnetic anisotropies with X-ray magnetic circular dichroism (XMCD) spectroscopy, *J. Magn. Magn. Mater.* **200**, 470 (1999).
- [68] T. Taniuchi, H. Kumigashira, M. Oshima, T. Wakita, T. Yokoya, M. Kubota, K. Ono, H. Akinaga, M. Lippmaa, M. Kawasaki, and H. Koinuma, Observation of step-induced magnetic domain formation in La_{1-x}Sr_xMnO₃ thin films by photoelectron emission microscopy, *Appl. Phys. Lett.* **89**, 112505 (2006).
- [69] S. S. Brinkman, X. L. Tan, B. Brekke, A. C. Mathisen, Ø. Finnseth, R. J. Schenk, K. Hagiwara, M.-J. Huang, J. Buck, M. Kalläne, M. Hoesch, K. Rossnagel, K.-H. Ou Yang, M.-T. Lin, G.-J. Shu, Y.-J. Chen, C. Tusche, and H. Bentmann, Chirality-driven orbital angular momentum and circular dichroism in CoSi, *Phys. Rev. Lett.* **132**, 196402 (2024).
- [70] X. L. Tan, A. Ernst, K. Hagiwara, Y. J. Chen, C. M. Schneider, and C. Tusche, Exchange Engineering of a Two-Dimensional Half-Metal, *Phys. Rev. Lett.* **135**, 036703 (2025).
- [71] Y.-J. Chen, C. Wiemann, W.-S. Chiu, C. Schlueter, C. M. Schneider, A. Phys Lett, and C. Tusche, Momentum microscopy and its applications, *Applied Physics Letters* **128**, 10503 (2026).
- [72] L. Šmejkal, J. Sinova, and T. Jungwirth, Emerging Research Landscape of Altermagnetism, *Phys. Rev. X* **12**, 040501 (2022).
- [73] R. Yamada, M. T. Birch, P. R. Baral, S. Okumura, R. Nakano, S. Gao, M. Ezawa, T. Nomoto, J. Masell, Y. Ishihara, K. K. Kolincio, I. Belopolski, H. Sagayama, H. Nakao, K. Ohishi, T. Ohhara, R. Kiyonagi, T. Nakajima, Y. Tokura, T. H. Arima, Y. Motome, M. M. Hirschmann, and M. Hirschberger, A metallic p-wave magnet with commensurate spin helix, *Nature* **646**, 837 (2025).

Supplemental Material: Electronic structure and resonant circular dichroism of $\text{La}_{0.7}\text{Sr}_{0.3}\text{MnO}_3$ from soft X-ray angle-resolved photoemission

Øyvind Finnseth¹, Damian Brzozowski¹,
Anders Christian Mathisen², Stefanie Suzanne Brinkman²,
Xin Liang Tan², Fabian Göhler², Benjamin A. D. Williamson¹,
Kristoffer Eggstad¹, Meng-Jie Huang^{3,4,5}, Jens Buck^{6,3,4}, Moritz
Hoesch⁵, Kai Rossnagel^{6,3,4,5}, Sverre M. Selbach¹,
Hendrik Bentmann², and Ingrid Hallsteinsen¹

¹*Department of Materials Science and Engineering, Norwegian University of Science and Technology, 7491 Trondheim, Norway*

²*Center for Quantum Spintronics, Department of Physics, Norwegian University of Science and Technology, 7491 Trondheim, Norway*

³*Ruprecht Haensel Laboratory, Kiel University, 24098 Kiel, Germany*

⁴*Ruprecht Haensel Laboratory, DESY, 22607 Hamburg, Germany*

⁵*Deutsches Elektronen-Synchrotron DESY, Notkestraße 85, 22607 Hamburg, Germany*

⁶*Institut für Experimentelle und Angewandte Physik, Christian-Albrechts-Universität zu Kiel, 24098 Kiel, Germany*

1 Sample growth and characterization

1.1 Sample growth

The $\text{La}_{0.7}\text{Sr}_{0.3}\text{MnO}_3$ thin film was grown by pulsed laser deposition (PLD) on (111)-oriented SrTiO_3 substrates (Shinkosha). Before growth, the substrate was cleaned in subsequent ultrasonic baths of acetone, ethanol and deionized water for 5 minutes each at room temperature followed by etching in a buffered hydrofluoric acid solution with a 1:9 ratio of HF to NH_4F for 1 minute. The substrate was annealed at 1050 °C under oxygen flow for 1 hour. Finally, once inserted into the PLD chamber, the substrate was annealed at 280 °C for 1 hour in a oxygen partial pressure of 0.3 mbar to remove organic contaminants from the surface. A KrF excimer laser with wavelength $\lambda = 248$ nm was used to ablate from a $\text{La}_{0.7}\text{Sr}_{0.3}\text{MnO}_3$ target (Kurt J. Lesker) at a target-substrate distance of 40 mm with a laser fluence of 1.2 J cm^{-2} . The laser frequency was set to 2 Hz. During growth, the sample was kept at 700 °C with an oxygen

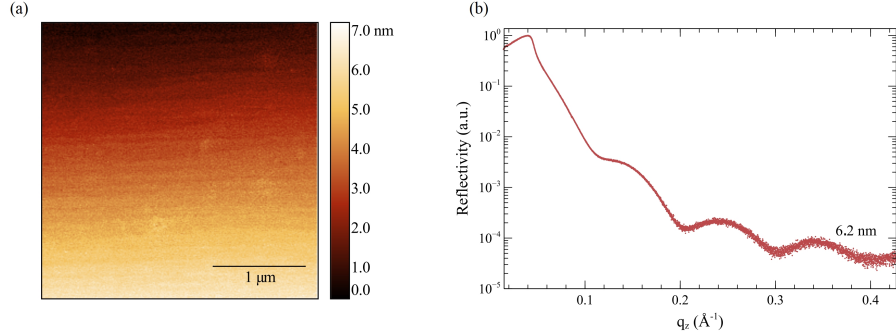


Figure 1: (a) AFM image of the LSMO thin film, showing a step-and-terrace structure. (b) X-ray-reflectivity profile of the LSMO thin film, with thickness fringes corresponding to a thickness of 6.2 nm.

background pressure of 0.12 mbar. After growth, the sample was annealed for 1 hour at 600 °C in 300 mbar O₂ partial pressure.

After growth, atomic force microscopy (AFM) images, shown in Fig. 1 (a), shows a smooth surface with step-terraces inherited from the SrTiO₃ substrate. A X-ray reflectivity profile was taken to determine the film thickness. This is shown in Fig. 1 (b), where the thickness fringes correspond to a film thickness of 6.2 nm.

1.2 Surface preparation

The sample was transported through air between the growth and the conducted ARPES measurements. As such, a surface preparation procedure was necessary upon reintroduction to vacuum. The procedure involved annealing the sample at temperature of ~ 640 K in O₂ gas with a partial pressure of 1×10^{-5} mbar. The efficacy of the preparation procedure was evaluated by X-ray photoelectron spectroscopy (XPS) and low energy electron diffraction (LEED). Fig. 2 (a) includes two XPS spectra from before and after the annealing procedure, respectively, and demonstrates the successful removal of C contamination and the emergence of the Sr 3p peaks. The XPS spectra were obtained using a Al K α source with photon energy $h\nu = 1486.6$ eV. In Fig. 2 (b), a LEED diffractogram taken after the preparation procedure indicates that a highly crystalline sample surface was obtained.

2 Effect of octahedral tilt pattern on calculated band structures

After optimizing the supercell geometry, the tilt of the O octahedra follows a $a^+b^-b^-$ pattern, such that the tilt along one axis is in-phase with the remaining

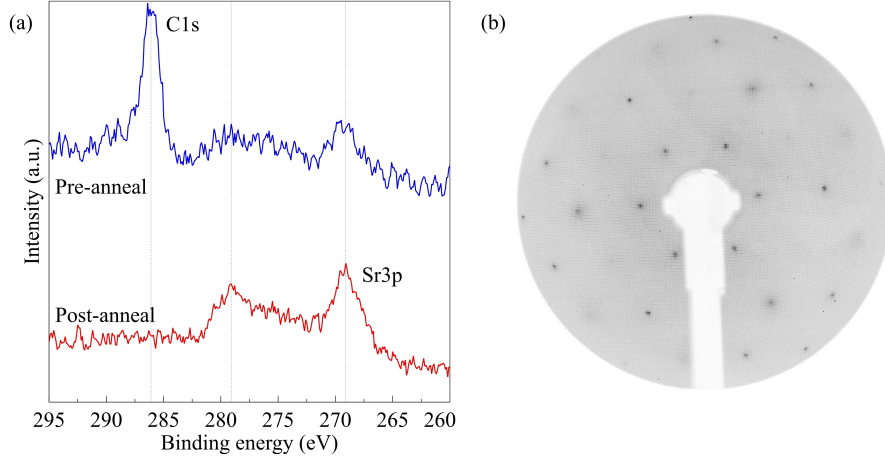


Figure 2: (a) XPS spectra of C 1s and Sr 3p peaks before (red) and after (blue) the surface preparation procedure, indicating the removal of C contamination and the emergence of Sr peaks. (b) LEED diffractogram taken after the preparation procedure with incident electrons with an energy of 156 eV, demonstrating that a well-ordered sample surface has been obtained.

two axes anti-phase. This deviates from the $a^-a^-a^-$ pattern in bulk LSMO, in which all axes exhibit anti-phase tilt patterns. The deviation is attributed to a small energy difference between the $a^+b^-b^-$ and $a^-a^-a^-$ geometries. In order to understand the impact of the deviating octahedral tilt, we here include calculated band structures for supercells in non-optimized geometries corresponding to the $R\bar{3}c$ and $Pm\bar{3}m$ space groups, respectively. In the case of the $R\bar{3}c$ space group, the octahedral tilt pattern is $a^-a^-a^-$, meaning anti-phase tilting of equal magnitude along all cubic axes. The resulting band structure is shown in Fig. 3 (a). we observe no significant differences from the band structure obtained for the supercell in an optimized geometry as shown in the main text. For the $Pm\bar{3}m$ supercell, there is no octahedral tilt. We observe that, as opposed to the supercells with octahedral tilt, the calculated band structure exhibits no mapping of the R-X plane to the Γ -M plane, indicating that this effect is indeed a result of the unit cell doubling along the [111] axis in the presence of octahedral tilt.

3 Circular dichroism

In Fig. 4 (d) in the main text, we compare the difference between the angle-integrated photoemission intensity for left and right circularly polarized light to the XMCD spectrum of LSMO. To see this clearly, consider the XMCD spectrum of the sample as shown in Fig. 4 (a) The XMCD spectrum exhibits the same step-wise peak at the L_3 resonance and double peak at the L_2 resonance,

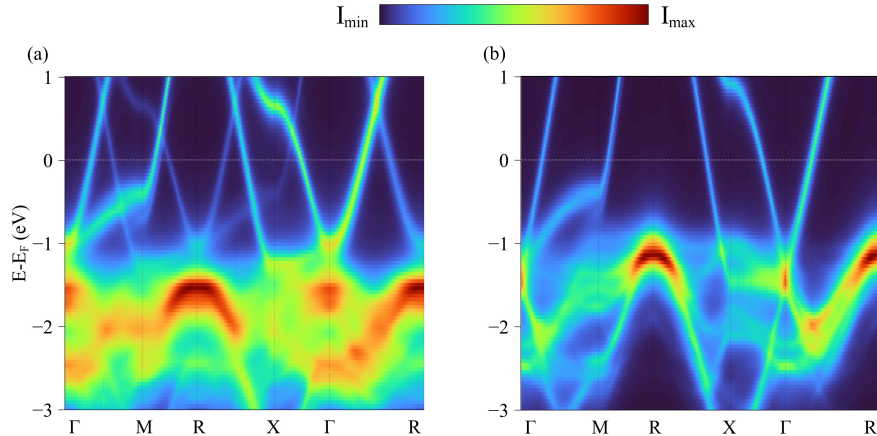


Figure 3: Spin up electronic band structures calculated by DFT+ U for a supercell with (a) $a^-a^-a^-$ octahedral tilt pattern as expected for the $R\bar{3}c$ space group and (b) for a supercell with no octahedral tilting.

along with the sign change between the two peaks. This indicates an in-plane ferromagnetic ordering in the sample.

To confirm the magnetic origin of the MCD discussed in the main text, we measured the photoemission CD for magnetization along $\pm M_x$, depicted in Fig. 4 (b). To switch the magnetization, the sample was magnetized *in-situ* at approximately 30 K using two oppositely oriented permanent magnets along x . When reversing the direction of the magnetization M_x , the sign of the angle-integrated photoemission CD likewise switches. The difference in the CD intensity between $\pm M_x$ is attributed to inconsistencies in the magnetization procedure.

The main text discusses the momentum-resolved magnetic circular dichroism (MCD) in resonant ARPES, obtained using a photon energy of $h\nu = 645$ eV. To explore the momentum distribution of the circular dichroism off resonance, we here include ARPES data measured with a photon energy of $h\nu = 475$ eV. In the integrated intensity $I = I_L + I_R$, shown in Fig. 5 (a), we observe a momentum distribution that appears mirror symmetric with respect to $k_y = 0$. Considering the circular dichroism $I_{CD} = I_L - I_R$, shown in Fig. 5 (b), we observe an anti-symmetric distribution. As discussed in the main text, this is in agreement with the distribution required by the crystallographic mirror plane along $k_y = 0$ in the absence of magnetic ordering. To confirm this, we extract the anti-symmetric and symmetric contributions to the total circular dichroism, shown in Figs. 5 (c) and (d), respectively. In contrast to the resonant MCD shown in Fig. 5 of the main text, we here observe that the total circular dichroism is dominated by the anti-symmetric contribution, with the symmetric contribution being negligible.

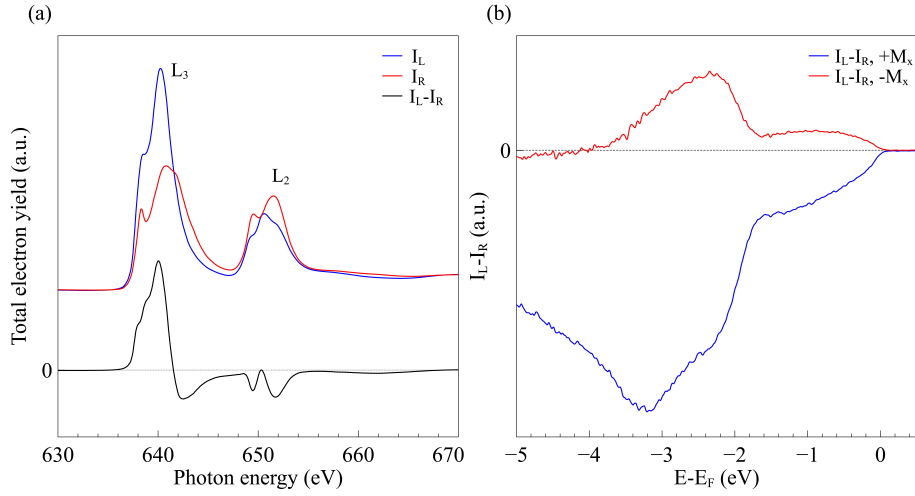


Figure 4: (a) XAS and XMCD spectra across the Mn L_3 and L_2 edges, indicating an in-plane ferromagnetic ordering in the sample. (b) Angle-integrated photoemission CD measured at the L_3 resonance for opposite magnetization directions $\pm M_x$ along the plane of light incidence. Switching the direction of the magnetization clearly switches the sign of the photoemission CD.

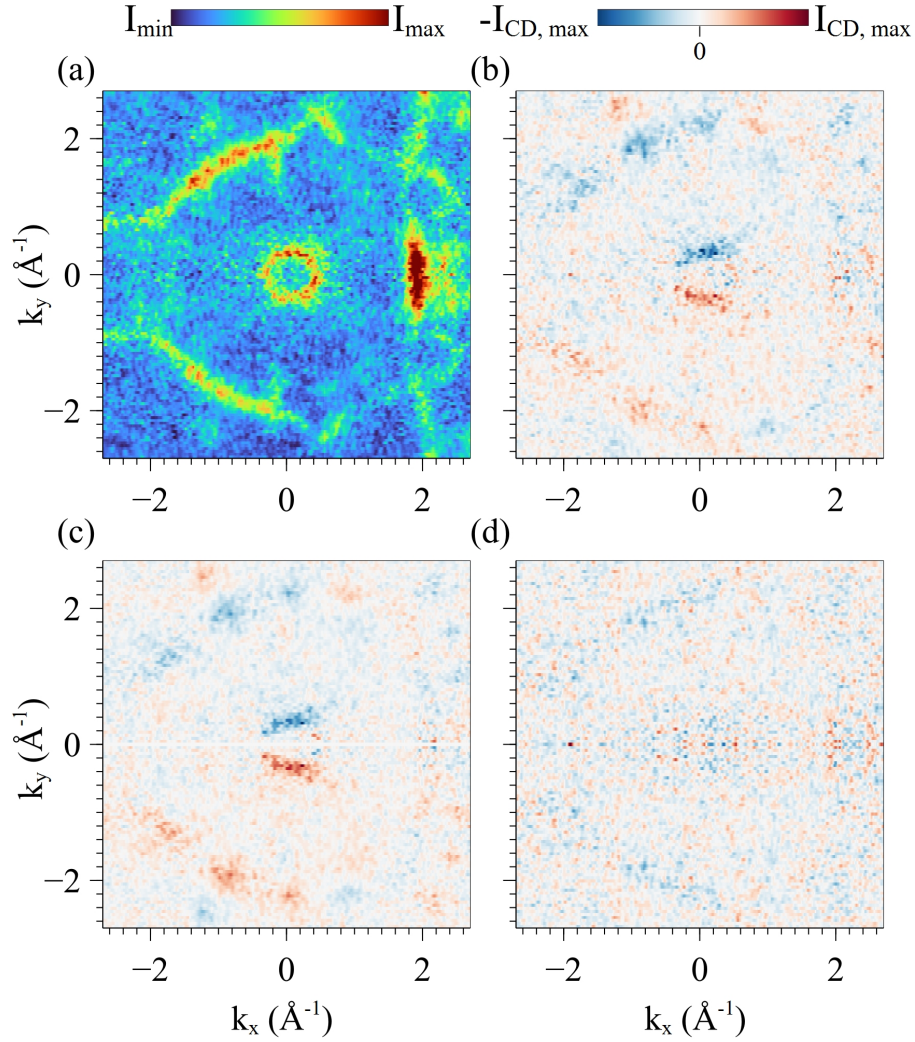


Figure 5: ARPES data measured at the Fermi level with $h\nu = 475$ eV. (a) Total intensity obtained as the sum of left and right circularly polarized light, $I = I_L + I_R$. (b) Circular dichroism obtained as the difference between left and right circularly polarized light $I_{CD} = I_L - I_R$. (c) Anti-symmetric contribution extracted from (b). (d) Symmetric contribution extracted from (b).